EXTREMELY ENERGETIC OUTFLOW AND DECELERATED EXPANSION IN W49N

Tie Liu[1], Kee-Tae Kim[1], Yuefang Wu[2], Di Li[3], Chang-Won Lee[1,4], Christopher G. De Pree[5], Sheng-Li Qin[6], Ke Wang[7], Ken'ichi Tatematsu[8], Qizhou Zhang[9], Diego Mardones[10], Sheng-Yuan Liu[11], and Se-Hyung Cho[1]

[1] Korea Astronomy and Space Science Institute 776, Daedeokdae-ro, Yuseong-gu, Daejeon 305-348, Korea; liutiepku@gmail.com
[2] Department of Astronomy, Peking University, 100871, Beijing, China
[3] National Astronomical Observatories, Chinese Academy of Science, A20 Datun Road, Chaoyang District, Beijing 100012, China
[4] University of Science and Technology, 217 Gajungro, Yuseong-gu, 305-333 Daejeon, Korea
[5] Department of Physics and Astronomy, Agnes Scott College, Decatur, GA 30030, USA
[6] Department of Astronomy, Yunnan University, and Key Laboratory of Astroparticle Physics of Yunnan Province, Kunming, 650091, China
[7] European Southern Observatory, Karl-Schwarzschild-Str. 2, D-85748 Garching bei München, Germany
[8] National Astronomical Observatory of Japan, 2-21-1 Osawa, Mitaka, Tokyo 181-8588, Japan
[9] Harvard-Smithsonian Center for Astrophysics, 60 Garden Street, Cambridge, MA 02138, USA
[10] Departamento de Astronomía, Universidad de Chile, Casilla 36-D, Santiago, Chile
[11] Institute of Astronomy and Astrophysics, Academia Sinica, Taipei, Taiwan

ABSTRACT

W49N is a mini-starburst in the Milky Way and is thus an ideal laboratory for high-mass star formation studies. Due to its large distance ($11.1^{+0.9}_{-0.7}$ kpc), the kinematics inside and between the dense molecular clumps in W49N are far from well-understood. The Submillimeter Array observations resolved the continuum emission into two clumps. The molecular line observation of SO_2 ($28_{4,24}$–$28_{3,25}$) suggests that the two clumps have a velocity difference of ~ 7 km s^{-1}. The eastern clump is very close to two radio sources "G1" and "G2," and the western clump coincides with a radio source "B." The HCN (3–2) line reveals an extremely energetic outflow, which is among the most energetic molecular outflows in the Milky Way. This is the first report of high-velocity molecular outflow detection in W49N. The outflow jet might be in precession, which could account for the distribution, velocity, and rotation of water maser spots. Three absorption systems are identified in HCO$^+$ (3–2) spectra. The absorption features are blueshifted with respect to the emission of SO_2 ($28_{4,24}$–$28_{3,25}$) lines, indicating that a cold layer is expanding in front of the warm gas. Further analysis indicates that the expansion is decelerated from the geometric expansion centers.

Key words: ISM: jets and outflows – ISM: kinematics and dynamics – stars: formation

1. INTRODUCTION

High-mass stars play a major role in the evolution of galaxies. When compared with their low-mass counterparts, the outflow parameters (e.g., masses, energy, and momentum) and mass infall rates in high-mass star formation regions are orders of magnitude larger (Zhang et al. 2001, 2005; Beuther et al. 2002; Wu et al. 2004; Qiu et al. 2008; Liu et al. 2013b), indicating that high-mass star formation is a more energetic process. Additionally, in contrast to isolated low-mass star formation, most high-mass stars form in clusters. However, the formation of high-mass stars is still far from clearly understood due to difficulties in observations caused by their large distances, clustered environments, short evolutionary timescales, and contamination from the feedback of protostars (Zinnecker & Yorke 2007). To study the physical and chemical environments of high-mass star-forming regions, high spatial resolution interferometric observations are required.

Located at a distance of $11.1^{+0.9}_{-0.7}$ kpc (Zhang et al. 2013), W49 is among the most luminous ($>10^7 L_\odot$) and massive ($\sim 10^6 M_\odot$) star-forming regions in the Milky Way (Sievers et al. 1991; Galván-Madrid et al. 2013), making it an ideal laboratory for high-mass star formation studies. As shown in the left panel of Figure 1, W49 contains three massive star-forming regions, W49 to the north (W49N), W49 to the south (W49S), and W49 to the southwest (W49SW), among which W49N is the most prominent one, containing 40–50 of UC H II regions which are arranged in a remarkable 2 pc diameter ring

("Welch ring") (Welch et al. 1987; De Pree et al. 1997; Smith et al. 2009). The "Welch ring" is shown in the upper right panel of Figure 1.

Several scenarios have been proposed to explain the triggering mechanism of the mini-starburst in W49N, including global collapse (Welch et al. 1987; Williams et al. 2004; Galván-Madrid et al. 2013), cloud–cloud collision (Mufson & Liszt 1977; Miyawaki et al. 1986; Tarter & Welch 1986; Serabyn et al. 1993; Buckley & Ward-Thompson 1996; De Pree et al. 1997), and expanding shells (Peng et al. 2010). The global collapse scenario was proposed based on the detection of redshifted absorption features ("inverse P-Cygni profile") in HCO$^+$ (1–0) (Welch et al. 1987) and CS (2–1) (Williams et al. 2004) lines. The cloud–cloud collision scenario is mainly based on the presence of overlapping clumps observed in molecular lines at different radial velocities (Serabyn et al. 1993; Buckley & Ward-Thompson 1996; De Pree et al. 1997). Peng et al. (2010) identified two expanding shells in the mid-infrared images and confirmed them with follow-up molecular line observations. They argued that the expanding shells in W49N are suggestive of triggered massive star formation in just $\sim 10^5$ years. Recently, Galván-Madrid et al. (2013) argued that the W49N starburst most likely formed from a global gravitational contraction with localized collapse in a "hubfilament" geometry through large mosaic mapping observations with the Submillimeter Array (SMA) in combination with single-dish observations. Previous works have indicated that W49N contains substructures and forms a cluster of OB stars. However, the kinematics and interactions of different
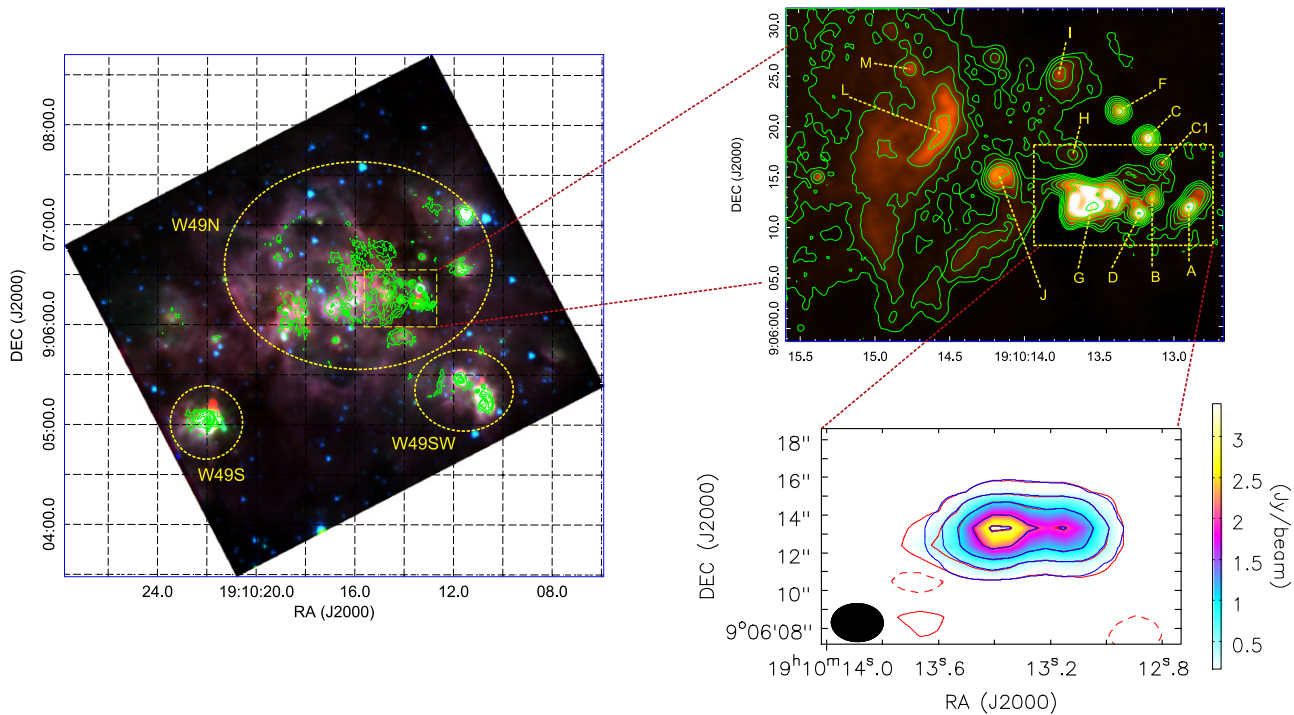
Figure 1. Left: the 3.6 cm continuum emission (De Pree et al. 1997) is shown in contours overlaid on the three color composite image from Spitzer/IRAC (3.6 μm in blue, 4.5 μm in green, and 8.0 μm in red). The contours start at the 3σ level (1.0 mJy beam^{-1}). Subsequent positive contours are at 2, 4, 8, 16, and 32 times the 3σ level. Upper right: the ring of UCH II regions ("Welch ring"). The color image and contours represent the 3.6 cm continuum emission. The names of the strongest UCH II regions are labeled. Lower right: the 1.1 mm continuum emission observed by the SMA is shown in the color image and red contours. The blue contours represent the two-dimensional Gaussian fits. The contours are $(5, 20, 50, 100, 150) \times 0.02$ Jy beam^{-1} (1 σ). The SMA beam is shown in filled black ellipse.

components in this region are still far from well-understood. In this paper, for the first time, we report the discovery of an extremely energetic outflow and localized expansion in the central region of W49N from the SMA observations with an angular resolution of $\sim2\rlap{.}''4$.

2. OBSERVATIONS

SMA data set is from the SMA[11] archive (Ho et al. 2004). The observations of W49N were carried out in 2005 September using the SMA's compact configuration. The phase reference center was R.A.(J2000) $= 19^{h}10^{m}13\rlap{.}^{s}41$ and decl.(J2000) $= 09°06'14\rlap{.}''30$. The 345 GHz receivers were tuned to 265 GHz for the lower sideband and to 275 GHz for the upper sideband. Each sideband has 3072 channels and a total bandwidth of ~2 GHz. The frequency spacing across the spectral band is 0.812 MHz or ~0.9 km s^{-1}. In the observations, QSOs 3C454.3, 1751+096, and the planet Uranus were observed for bandpass correction, antenna-based gain correction, and flux-density calibration, respectively.

The software package Multichannel Image Reconstruction, Image Analysis and Display (MIRIAD) was employed for calibration and imaging (Sault et al. 1995). The 1.1 mm continuum data were acquired by averaging all of the line-free channels over both the upper and lower spectral bands. MIRIAD task "selfcal" was employed to perform self-calibration on the continuum data. The gain solutions from the self-calibration were applied to the line data.

The primary beam of the SMA at 270 GHz is $\sim40''$. The uv distances range from 10 to 62 $k\lambda$. The synthesized beam size and 1 σ rms of the continuum emission are $2\rlap{.}''77 \times 2\rlap{.}''02$ (PA $= 88\rlap{.}°9$) and ~20 mJy beam^{-1}, respectively. We smoothed the spectral lines to a spectral resolution of 1 km s^{-1} and the corresponding 1σ rms for lines is ~0.1 Jy beam^{-1} per channel.

3. RESULTS

3.1. 1.1 mm Continuum Emission

The 1.1 mm continuum image is shown in red contours and a color image in the lower right panel of Figure 1. Two clumps are revealed in the 1.1 mm continuum emission. The 1.1 mm continuum emission can be well-fitted with two two-dimensional Gaussian sources as shown in blue contours. The peak positions of the eastern and western clumps are $(-0\rlap{.}''35 \pm 0\rlap{.}''09, -1\rlap{.}''13 \pm 0\rlap{.}''03)$ and $(-4\rlap{.}''06 \pm 0\rlap{.}''13, -1\rlap{.}''09 \pm 0\rlap{.}''06)$ offset from the phase center, respectively. The total integrated flux and deconvolved size of the eastern clump are 4.40 Jy and $2\rlap{.}''04 \times 0\rlap{.}''71$ (P.A. $= -74\rlap{.}°7$), respectively. Assuming a distance of 11.1 kpc, the effective radius of the eastern clump, which is defined as $\sqrt{ab}$, where a and b are the FWHM deconvolved sizes of major and minor axes, is ~0.065 pc. The western clump is not resolved by the SMA and appears to be a point source with a total integrated flux of 2.02 Jy. In the upper panel of Figure 2, we present the 3.6 cm continuum emission (De Pree et al. 1997) as a color image and also label the previously discovered bright radio continuum sources. We find that the eastern continuum emission peak is very close to two radio sources "G1" and "G2." The western continuum emission peak coincides with a radio source "B."
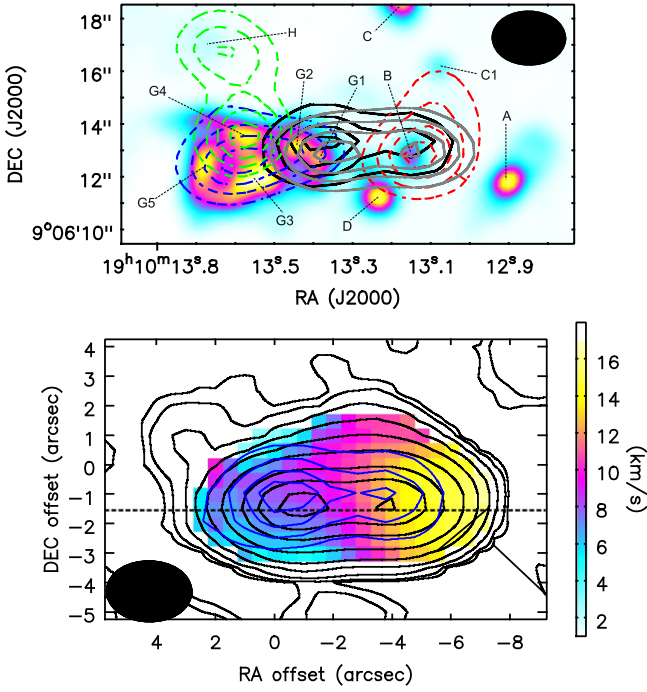
Figure 2. Upper panel: the 3.6 cm continuum emission (De Pree et al. 1997) is shown in a color image. The names of bright cm continuum sources are labeled from "A" to "H." The integrated intensity maps of "-7.5," "2.0," and "12.5 km s^{-1}" absorption of HCO$^+$ (3–2) are shown in the green, blue, and red dashed contours, respectively. The 1.1 mm continuum emission and integrated intensity map of SO$_2$ ($28_{4,24}$–$28_{3,25}$) are shown in the solid black and gray contours, respectively. All of the contours are started from 30% in step of 20% of the peak values. The peak values for the green, blue, red, gray, and black contours are -12.8, -19.8, -8.7, 106.2 Jy beam^{-1} km s^{-1}, and 3.2 Jy beam^{-1}, respectively. Lower panel: the intensity-weighted velocity (Moment 1) map of SO$_2$ ($28_{4,24}$–$28_{3,25}$) is shown in a color image. The integrated intensity map of SO$_2$ ($28_{4,24}$–$28_{3,25}$) is shown in black contours. The contours are $[-3, 3, 5, 10, 20, 40, 80, 160, 240, 320] \times 0.3$ Jy beam km s^{-1} (3 σ). The 1.1 mm continuum emission is shown in blue contours. The SMA beam is shown in the filled black ellipse.

3.2. Line Emission

Dozens of molecular lines were detected in both sidebands and were identified with the Splatalogue database for astronomical spectroscopy. Here we report the results from SO$_2$ ($28_{4,24}$–$28_{3,25}$), HCN (3–2), and HCO$^+$ (3–2) lines.

3.2.1. SO$_2$ ($28_{4,24}$–$28_{3,25}$) Emission

The integrated intensity from -10 to 30 km s^{-1} of SO$_2$ ($28_{4,24}$–$28_{3,25}$) is shown in gray contours in the upper panel and black contours in the lower panel of Figure 2, respectively. The emission of SO$_2$ ($28_{4,24}$–$28_{3,25}$) coincides with the 1.1 mm continuum emission very well. From its intensity-weighted velocity map (moment 1) in the lower panel of Figure 2, one can see that there is a large velocity gradient from east to west. This large velocity gradient is more clearly seen from the position–velocity diagram of SO$_2$ ($28_{4,24}$–$28_{3,25}$) (Figure 3), which is cut along the black dashed line in the lower panel of Figure 2. The peak velocities of SO$_2$ ($28_{4,24}$–$28_{3,25}$) are estimated from Gaussian fits at the individual positions and are marked with blue crosses in the lower panel of Figure 3. The peak velocities of SO$_2$ ($28_{4,24}$–$28_{3,25}$) at the continuum emission peaks of the eastern and western clumps are 5.8 ± 0.1 and 12.7 ± 0.1 km s^{-1}, respectively. The velocity gradient between these two clumps is ~ 34.7 km s^{-1} pc^{-1}.
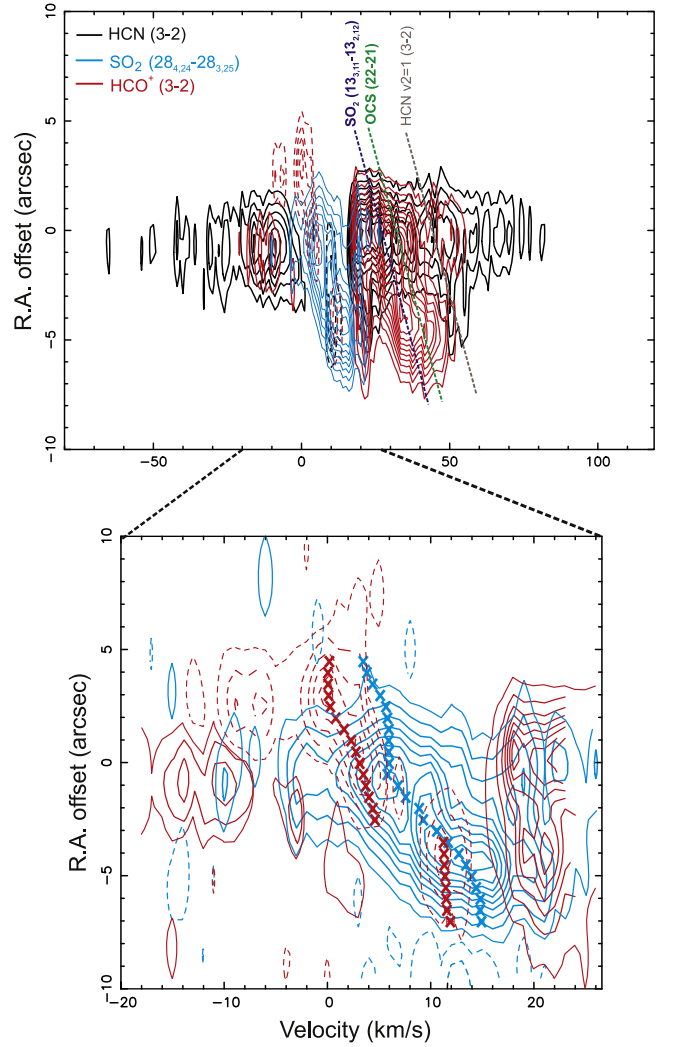

Figure 3. Position–velocity diagrams of HCN (4–3), SO$_2$ ($28_{4,24}$–$28_{3,25}$) and HCO$^+$ (3–2) are shown in the black, blue, and red contours, respectively. The Position–Velocity diagrams are made by cutting along the black dashed line in Figure 2. The R.A. offsets are relative to 19^h10^m1341. All of the contours in the upper panel are started from 1 Jy beam^{-1} (10 σ) in step of 1 Jy beam^{-1}. All of the contours in the lower panel are started from 0.3 (3 σ), 1 Jy beam^{-1} in step of 1 Jy beam^{-1}. The dashed straight lines in the upper panel represent the contaminated molecular lines (SO$_2$ ($13_{3,11}$-$13_{2,12}$), OCS (22-21), and HCN v2 = 1 (3–2)). These dashed straight lines are oblique due to the velocity gradient. The red and blue crosses in the lower panel mark the peak velocities of SO$_2$ ($28_{4,24}$–$28_{3,25}$) emission lines and HCO$^+$ (3–2) absorption lines at each position from Gaussian fits.

3.2.2. Extremely High Velocity Emission in HCN (3–2) Lines

As shown in the position–velocity diagram (upper panel of Figure 3) and averaged spectrum (upper panel of Figure 4), the HCN (3–2) line emission shows extremely high-velocity emission. The terminal velocities of the blueshifted and redshifted emission are as high as ~ -70 and ~ 90 km s^{-1}, respectively. The redshifted high-velocity emission is contaminated by the HCN v2 = 1 (3–2) line, located at around 50 km s^{-1}, as marked by the dashed dark brown line in the position–velocity diagram. There is also an emission peak in the averaged spectrum of HCN (3–2) (upper panel of Figure 4) at around 50 km s^{-1} due to the contamination of the HCN v2 = 1 (3–2) line. To confirm the contamination of HCN v2 = 1 (3–2), we integrated emission from 49 to 51 km s^{-1} and
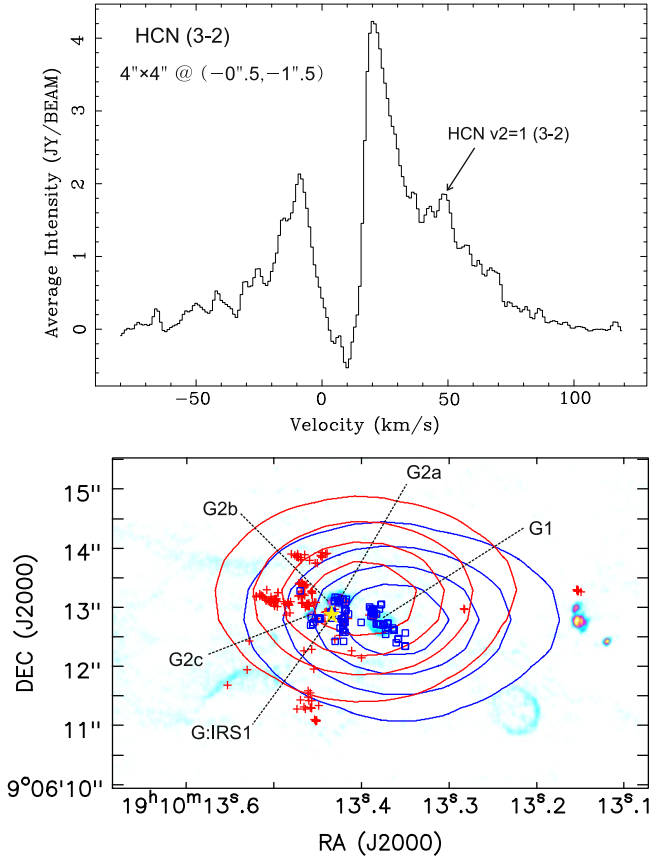
Figure 4. Upper panel: spectrum of the HCN (3–2) line, which is averaged over a $4'' \times 4''$ area centered at the position $(-0\rlap{.}''5, -1\rlap{.}''5)$, offset from the phase reference center. Lower panel: the 7 mm continuum emission (De Pree et al. 2000) is shown in a color image. The integrated intensity maps of high-velocity blueshifted and redshifted emission of HCN (3–2) are shown in the blue and red contours. The red crosses and blue boxes mark the positions of water masers with positive and negative LSR velocities, respectively. All the contours are started from 20% in step of 20% of the peak values. The peak values for the blue and red contours are 30, and 49.4 Jy beam^{-1} km s^{-1}, respectively. The mid-IR source "G:IRS1" is marked with a yellow filled star.

present the integrated intensity in Figure 5 as a color image and white contours. The spatial distribution of the HCN v2 = 1 (3–2) emission, while contaminated by HCN (3–2) high-velocity emission, is roughly consistent with the 1.1 mm continuum but is significantly different from outflow emission, as shown in Figure 4. The integrated intensity map in Figure 5 also rules out the possibility of contamination emission from foreground clouds, which would show a very extended structure if it existed.

Roberts et al. (2011) observed the J = 3–2 and 4-3 transitions of HCN with the James Clerk Maxwell Telescope (JCMT) toward W49N. However, due to poor angular resolution and sensitivity, they did not detect such high-velocity wings. Their spectral lines can be well-fitted with two gaussian components, indicating the existence of substructures. The HCN outflow discovered in this work should be the first report of high-velocity outflow detection in W49N. We divide the outflow emission into "Low" and "High" components. The velocity intervals for each component are shown in the second column of Table 1. The emission between 40 and 60 km s^{-1} is not included in further analysis due to the contamination of the HCN v2 = 1 (3–2) line. The integrated intensity maps of the blueshifted and redshifted "High" outflow emission are shown
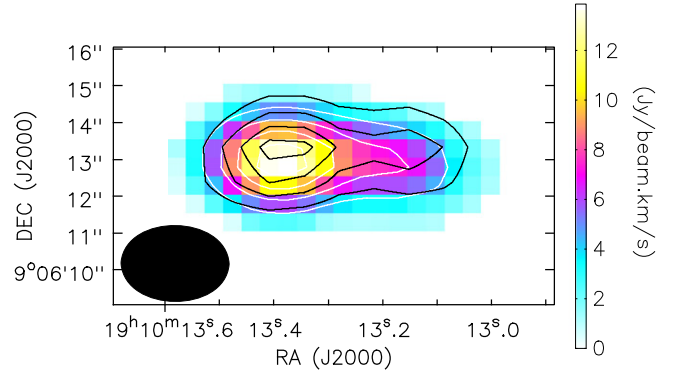

Figure 5. Integrated intensity of the HCN v2 = 1 (3–2) line shown as white contours and a color image. The 1.1 mm continuum emission is shown in the black contours. All of the contours are started from 20% in step of 20% of the peak values. The peak value of HCN v2 = 1 (3–2) is 13.9 Jy beam^{-1} km s^{-1}.

as blue and red contours, respectively, in the lower panel of Figure 4. The blueshifted and redshifted outflow emission overlaps and only displaces by $0\rlap{.}''7$ ($\Delta\theta$) in projection, indicating the outflow axis is almost along the line of sight (LOS). The projection deconvolved angular size of minor axes of outflow lobes is about $2''$ (θ). The upper limit of the outflow inclination angle with respect to the LOS is $\varphi = \frac{\Delta\theta}{\theta} = \frac{0.7}{2} \times \frac{180°}{\pi} \simeq 20°$. The characteristic outflow velocity (V_{char}) is defined as $V_{char} = V_{flow} - V_{sys}$, where V_{sys} is the systemic velocity (5.8 km s^{-1}) of the eastern continuum clump and V_{flow} is the intensity-weighted velocity of high-velocity emission corrected with the projection effect by assuming an outflow inclination angle of 20°. The characteristic outflow velocity of each outflow component is presented in the third column of Table 1. The V_{char} of the high-velocity redshifted outflow ("High Red") component is as high as 71.5 km s^{-1}, indicating that the outflow is extremely energetic. The effective emission radius of each outflow component shown in the fourth column of Table 1 is derived from its deconvolved size and also corrected with the projection effect. The effective radii of the emission areas of the "Low" and "High" outflow components are 0.1 and 0.2 pc, respectively. The outflow properties will be discussed in detail in Section 4.2.

3.2.3. Absorption in HCO$^+$ (3–2) lines

Figure 6 presents spectra of HCO$^+$ (3–2) and SO$_2$ ($28_{4,24}$–$28_{3,25}$) at six positions. Three absorption systems in HCO$^+$ (3–2) lines are identified. The mean velocities of these three absorption systems are "-7.5 km s^{-1}," "2.0 km s^{-1}," and "12.5 km s^{-1}," respectively. These three absorption systems can also be clearly seen from the position–velocity diagrams in Figure 3 as in dashed contours. We made the integrated intensity maps in the velocity intervals of $[-10, -4]$, $[-2, 6]$, and $[10, 15]$ km s^{-1} for the "-7.5," "2.0," and "12.5 km s^{-1}" absorption systems, respectively, and display them as the dashed contours in the upper panel of Figure 2. The "-7.5 km s^{-1}" absorption is associated with radio continuum sources "H" and "G4." The "-2.0 km s^{-1}" absorption perfectly corresponds to the 3.6 cm continuum emission of "G," which includes sources "G1" to "G5." The "12.5 km s^{-1}" absorption is associated with radio source "B." Additionally, from the spectra in Figure 6 and the position–velocity diagram in Figure 3, one can see that HCO$^+$ (3–2) absorption dips are always at the blueshifted side of the SO$_2$ ($28_{4,24}$–$28_{3,25}$)

Table 1
Outflow Parameters Derived from HCN (3–2) Lines

Component	Velocity Interval (km s^{-1})	V_{char}[a] (km s^{-1})	R_{eff}[a] (pc)	t (10^3 year)	M ($M_\odot$)	P ($M_\odot \cdot$ km s^{-1})	E (10^{47} erg)	$\dot{M}$ (10^{-4} $M_\odot$ yr^{-1})	L_m (10^2 $L_\odot$)
Low Blue	[−30, −10]	26.2	0.1	10.9	12	300	0.8	0.6	0.6
Low Red	[30, 40]	29.5	0.1	7.8	12	350	1.0	0.9	1.1
High Blue	[−80, −30]	55.7	0.2	6.2	6	340	1.9	1.1	2.6
High Red	[60, 120]	71.5	0.2	4.8	10	710	5.0	3.0	8.7

Note.
[a] Corrected with an inclination angle of 20° with respect to the line of sight. R_{eff} is the FWHM deconvolved size.

emission except in the overlapped regions (e.g., $(-1''.5, -1''.5)$ and $(-2''.5, -1''.5)$ off positions) of the two clouds. The HCO$^+$ (3–2) spectra in the right column of Figure 5 have a typical "P-Cygni" profile with emission peaks redshifted with respect to absorption dips. The peak velocities of HCO$^+$ (3–2) absorption dips estimated from Gaussian fits at each position are also marked with red crosses in the lower panel of Figure 3. One can see that the absorption dips of HCO$^+$ (3–2) are mostly blueshifted to the emission peaks of SO$_2$ ($28_{4,24}$–$28_{3,25}$). Since SO$_2$ ($28_{4,24}$–$28_{3,25}$) ($E_u \sim 416$ K) has a much higher upper energy level than that of HCO$^+$ (3–2) ($E_u \sim 26$ K), this velocity placement indicates that HCO$^+$ (3–2) absorption traces an localized expanding cold layer in front of the warm gas traced by SO$_2$ ($28_{4,24}$–$28_{3,25}$) emission. More discussion about the absorption in HCO$^+$ (3–2) lines will be presented in Section 4.2.

4. DISCUSSION

4.1. Extremely Energetic Molecular Outflow

4.1.1. The outflow properties

As presented in Section 3.2.2, the HCN (3–2) lines show extremely high-velocity emission, indicating energetic outflows. Following Liu et al. (2011a), the total mass of each outflow lobe is given by:

$$M = 1.04 \times 10^{-4} D^2 \frac{Q_{rot} e^{E_u/T_{rot}}}{\chi \nu^3 S \mu^2} \int \frac{\tau}{1 - e^{-\tau}} S_\nu dv, \quad (1)$$

where M, D, S_ν, χ, and τ are the outflow gas mass in $M_\odot$, the source distance in kiloparsecs, the line flux density in Jy, the fractional abundance with respect to H$_2$, and the optical depth, respectively. Q_{rot}, E_u, T_{rot}, ν, S, and μ are the rotational partition function, the upper level energy in K, the rotation temperature, the rest frequency, the line strength, and the permanent dipole moment, respectively. Owing to the lack of a direct estimation of the fractional abundance of HCN in the outflow region of W49N, we adopt the same fractional abundance of 5.2×10^{-9} as that in G9.62+0.19 F (Liu et al. 2011a) in calculating the outflow parameters. Assuming that the high-velocity emission is optically thin and $T_{rot} = 30$ K (Liu et al. 2011a), the outflow masses were calculated and presented in the sixth column of Table 1. The total outflow mass is ~40 $M_\odot$. The momentum can be calculated by $P = M \times V_{char}$, and the energy by $E = \frac{1}{2}M \times V_{char}^2$. The momentum and energy of the outflows are shown in the seventh and eighth columns, respectively. The total momentum and energy are 1700 $M_\odot$ km s^{-1} and 8.7×10^{47} erg, respectively. The dynamical

timescale t is estimated as $2R_{eff}/V_{char}$ and presented in the fifth column of Table 1. The dynamic timescale is about 0.5–1×10^4 year. In comparison with surveys of molecular outflows in massive star-forming regions (Zhang et al. 2001, 2005), the outflow mass, momentum, and energy in W49N are in the upper bound of the outflow parameters of massive star formation.

The mechanical luminosity L_m, and the mass-loss rate $\dot{M}$ are calculated as $L_m = E/t$ and $\dot{M} = P/(tV_w)$. Here we assume that the outflow is powered by winds driven by accretion disks and the wind velocity V_w is 500 km^{-1} (Zhang et al. 2005). The mechanical luminosity and the mass-loss rates are listed in the last two columns of Table 1. The total mechanical luminosity and the mass-loss rate of the outflows are estimated to be 1.3×10^3 $L_\odot$ and 5.6×10^{-4} $M_\odot \cdot$ yr^{-1}, respectively. Assuming that only one-third of the accreted mass is ejected in winds (Shu et al. 1987), we find a lower limit to the accretion rate to be 1.7×10^{-3} $M_\odot \cdot$ yr^{-1}.

Smith et al. (2009) identified a mid-infrared (IR) source (G: IRS1) and assigned it to the driving source of the outflow. From SED modeling, they inferred that the embedded protostar has a stellar mass of ~45 $M_\odot$, a luminosity of ~3×10^5 $L_\odot$, and an equivalent envelope accretion rate of ~10^{-3} $M_\odot$ yr^{-1}. The mechanical luminosity of O type stars with a mass-loss rate of $\dot{M}$ and stellar wind velocity v_w can be estimated from (Nagy et al. 2012):

$$L_w = 1.3 \times 10^{36} \left(\frac{\dot{M}}{10^{-6} M_\odot \text{ yr}^{-1}}\right) \left(\frac{v_w}{2 \times 10^3 \text{km s}^{-1}}\right)^2 \text{erg s}^{-1}.$$
$$(2)$$

The mechanical luminosity of an O type star with a mass-loss rate of $10^{-6} M_\odot$ yr^{-1} and a stellar wind velocity of 2000 km s^{-1} (Smith 2006) is ~340 $L_\odot$. Assuming an efficiency of 10%, its mechanical heating rate (34 $L_\odot$) is much smaller than the mechanical luminosity (1.3×10^3 $L_\odot$) of outflows, indicating that the outflow could not be driven by the stellar winds of a single O type star (e.g., G:IRS1). The outflow might be driven by accretion as suggested by Smith et al. (2009). The envelope accretion rate is in their model fits to the infrared spectral energy distribution (IR SED) is 1×10^{-3} $M_\odot \cdot$ yr^{-1} (Smith et al. 2009), which is consistent with the accretion rate (1.7×10^{-3} $M_\odot \cdot$yr^{-1}) inferred from the HCN outflow.

There are large uncertainties in the estimation of the outflow parameters. The optically thin assumption may not be true for low-velocity outflows. Assuming an average optical depth of 1.5, the corresponding outflow parameters (M, P, E, $\dot{M}$, and L_m) will become two times larger. As mentioned before, we
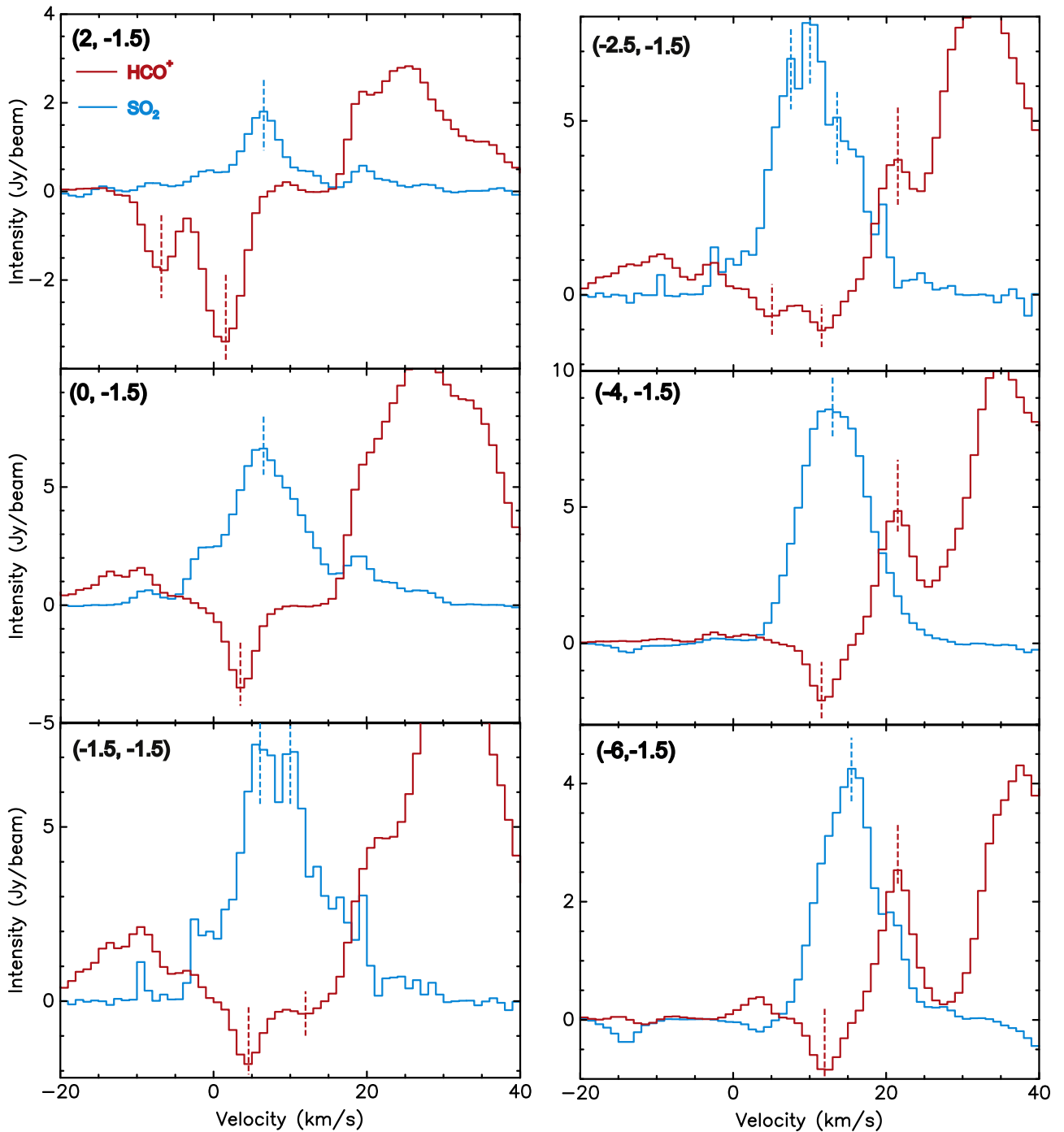
Figure 6. Spectra of HCO$^+$ (3–2) and SO$_2$ ($28_{4,24}$–$28_{3,25}$) at six positions (labeled at the upper right corner of each panel in unit of arcseconds, and take along the line shown in Figure 2-bottom.) are shown in red and blue, respectively. The velocities of the absorption dips of HCO$^+$ (3–2) and emission peaks of HCO$^+$ (3–2) and SO$_2$ ($28_{4,24}$–$28_{3,25}$) are marked with red and blue dashed vertical lines, respectively.

ignored the emission at velocities between 40 and 60 km s^{-1} due to the contamination of the HCN v2 = 1 (3–2) line, which definitely leads to an underestimation of the outflow parameters for redshifted high-velocity emission. The outflow parameters are less sensitive to the temperature. If we take a rotation temperature of 60 K (two times larger than the value we used), the outflow parameters only become 30% smaller. The largest uncertainties come from the fractional abundance of the HCN and inclination angle. Roberts et al. (2011) derived an H$_2$ volume density n$_{H_2}$ of 2×10^6 cm^{-3} and an HCN column density of $(2$–$7) \times 10^{15}$ cm^{-2} in the "Core" region of W49N.

The angular size of the HC^{15}N (4–3) emission is $L \sim 23''$. We can estimate an average H$_2$ column density: $N_{H_2} = L \times N_{H_2} = 7.6 \times 10^{24}$ cm^{-2}. Therefore, the fraction abundance of HCN at "Core" region is $(2.6$–$9.2) \times 10^{-10}$, which is about one order of magnitude smaller than the value (5.2×10^{-9}) we used, indicating that the outflow parameters could be significantly underestimated. However, HCN appears to be greatly enhanced in some outflow regions. In the NGC 1333 IRAS 2A outflow region, the fractional abundance of HCN is about two times larger than that in the core region (Jørgensen et al. 2004), while in the L1157 outflow region, the HCN abundance is even

further enhanced, by a factor of 100. Thus, a more accurate determination of the HCN abundance in outflow regions is critically important for estimating outflow parameters. Su et al. (2007) estimated an HCN abundance of $1–2 \times 10^{-8}$ in the massive outflow lobes of IRAS 20126+4104. If we assume that HCN fractional abundance in W49N is 1×10^{-8} as in IRAS 20126+4104 outflows, the outflow parameters will become about two times smaller. The inclination angle directly affects the estimation of R_{eff} and V_{char}. The outflow parameters of M, P, and E do not change too much ($<10\%$) when the inclination angle changes from $10°$ to $30°$, while the corresponding $\dot{M}$ and L_m can change by a factor of 2. In general, the respective uncertainty of outflow parameters due to the effects discussed above could be at least one order of magnitude. The outflow in W49N was not detected in CO (2–1) line emission with an angular resolution of $3''$ (Galván-Madrid et al. 2013). The reason may be that the outflow is very compact and warm, which cannot be revealed with low excitation lines. Further higher angular resolution and higher sensitivity observations of multiple higher excitation transitions of HCN and other molecular lines (e.g., CO, SiO) may help to better constrain the outflow properties.

HCN outflows have been detected by interferometers toward several other high-mass star-forming regions (Su et al. 2007; Liu et al. 2010, 2013a, 2011b, 2011a; Zhu et al. 2011). Compared with those outflows, W49N has a much larger outflow velocity. Among the previous detected HCN outflows, the one in G9.62+0.19 F might be the most energetic one (Liu et al. 2011a). The outflow in W49N has a similar mass and momentum to those of G9.62+0.19 F, but the energy and mechanical luminosity are about 10 times larger. Wu et al. (2004) cataloged 391 outflows, most of which were detected by single dishes. When compared with those outflows, the one in W49N is also among the most luminous and energetic outflows. The maximum energy and mechanical luminosity of the outflows in Wu et al. (2004) are around 10^{48} erg and 10^3 $L_{\odot}$, respectively, which are comparable to those in W49N. Thus, we argue that the outflow in W49N is among the most energetic outflows in the Milky Way. However, we should caution that the HCN outflow is barely resolved by the SMA and may contain multiple outflows, as seen in other high-mass cluster forming regions (e.g., NGC7538S; Naranjo-Romero et al. 2012). Therefore, the outflow parameters estimated here may be the sum of multiple outflows.

4.1.2. Does the Outflow Excite the Water Masers?

W49N harbors the most luminous water maser activities in the Milky Way (Walker et al. 1982). The water masers in W49N are mainly located near the H II regions "G1" and "G2" (Moran et al. 1973; Walker et al. 1982; Gwinn et al. 1992; De Pree et al. 2000; Mcgrath et al. 2004). Mcgrath et al. (2004) identified 316 water maser components with a velocity spanning from −352.1 to 375.5 km s^{-1}. In the lower panel of Figure 4, we overlay the water maser spots on the integrated intensity contours of HCN (3–2) high-velocity outflow emission. The water maser spots near "G1" and "G2" are distributed in three distinct clusters. Those maser spots with blueshifted and redshifted high-velocity features are located to the west and to the east of the mid-IR source "G:IRS1," respectively. The tightest cluster of maser spots is close to "G:IRS1" and has a linear arrangement elongated along a north–south axis. Honma et al. (2004) detected a strong maser

outburst on an arc-like structure in the central cluster, which may be due to a shock phenomenon powered by a forming star or a star cluster. Recently, from proper motion measurements, Zhang et al. (2013) found that those water maser spots appear to be in expansion and rotation with expanding and rotating velocities of 10.99 ± 1.33 and 5.28 ± 0.80 km s^{-1}.

The water maser emission in W49N has been a puzzle to astronomers for decades. Tarter & Welch (1986) suggested a cloud–cloud collision model for water maser excitation in W49N. An alternative and promising explanation is that water masers form at the edge of the outflow cavity walls (or jet-driven cocoons; Mac Low et al. 1994; Smith et al. 2009). Such a model for water maser excitation requires a shock velocity on the cavity walls of ~ 20–200 km s^{-1}. Since the outflow velocity of HCN (3–2) is up to ~ 70 km s^{-1}, water masers should be easily excited at the edge of the outflow cavity walls. Additionally, the low inclination angle of the outflow might account for the observed high-velocity features of water masers. As mentioned before, the blueshifted and redshifted high-velocity emission of HCN (3–2) overlaps and is only displaced by $\sim 0''7$ in projection, which is not resolved by the SMA. However, the orientation of the HCN outflow is roughly consistent with the water maser outflow. The western cluster of water masers is located at the peak of the blueshifted high-velocity HCN emission. While the eastern cluster of water maser emission is mainly at the red lobe of HCN outflow. A ~ 25 km s^{-1} CO outflow was observed by Scoville et al. (1986), where the blueshifted CO emission is toward the east and the redshifted CO emission is to the west. The orientation for the low-velocity CO outflow is opposite to the high-velocity HCN outflow, indicating that the outflow jet might be in precession. The jet precession naturally explains why the high- and low-velocity features coexist in the central cluster of water masers, while at the western and eastern clusters of waters masers, only high-velocity features are observed (Mcgrath et al. 2004). The expansion of the water maser spots might be caused by outflows. The jet precession can naturally explain why the maser spots are also in rotation in spite of expansion. However, we should point out that the jet precession scenario needs to be tested by higher angular resolution observations because: (1) the outflow in W49N is not obvious in new CO (2–1) line observations with the SMA Galván-Madrid et al. (2013); (2) the HCN outflow is barely resolved by the SMA and may contain multiple outflows.

4.2. Decelerated Expansion?

As discussed in section 3.2.3, the absorption dips of HCO$^+$ (3–2) are all blueshifted with respect to the emission peaks of SO$_2$ ($28_{4,24}$–$28_{3,25}$), indicating that the cold layers may be in expansion. Since there is no SO$_2$ ($28_{4,24}$–$28_{3,25}$) emission corresponding to the "-7.5 km s^{-1}" absorption system, here we only focus on the "2.0" and "12.5 km s^{-1}" absorption systems. The systemic velocities of the warm layers can be determined from SO$_2$ ($28_{4,24}$–$28_{3,25}$) emission lines. We define the LOS expansion velocity V_{exp}^{los} as $V_{exp}^{los} = V_{emi} - V_{abs}$, where V_{emi} is the velocity of the emission peak of SO$_2$ ($28_{4,24}$–$28_{3,25}$) and V_{abs} is the velocity of the absorption dip of HCO$^+$ (3–2). V_{emi} and V_{abs} were derived from Gaussian fits and marked with blue and red crosses in the position–velocity diagram in the lower panel of Figure 3, respectively. We derive V_{exp}^{los} at different positions along the black dashed line in the lower panel of Figure 2 and plot V_{exp}^{los} versus the R.A. offsets in the
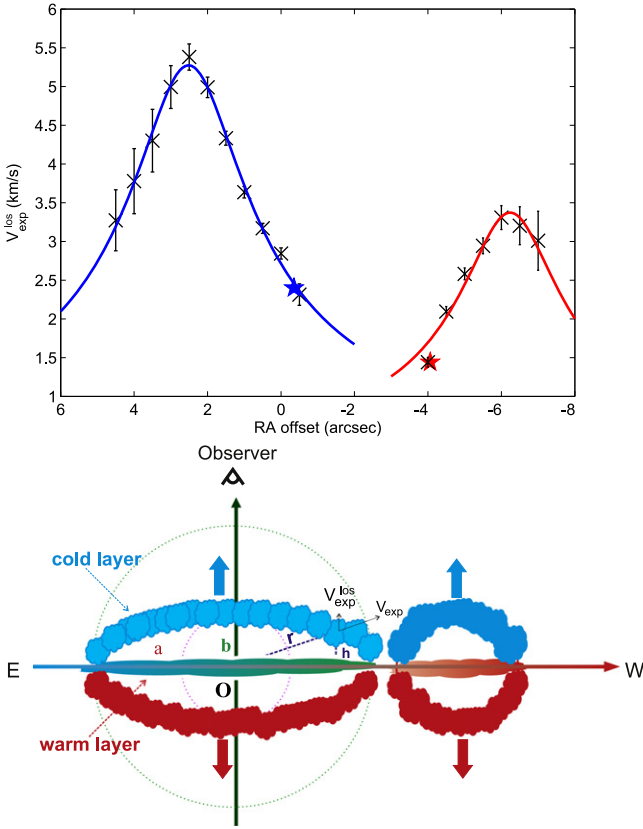
Figure 7. Lower panel: a cartoon of one possible geometric model for causing the absorption in HCO$^+$ (3–2) lines in W49N. There are two expanding systems. The cold gas traced by HCO$^+$ (3–2) absorption is distributed in two parallel expanding elliptical layers. The warm gas traced by SO$_2$ ($28_{4,24}$–$28_{3,25}$) is distributed along the middle plane. The color change of the horizon axis reflects the velocity gradient in SO$_2$ ($28_{4,24}$–$28_{3,25}$) emission. The maximum height ("h") of the cold layer is "b," and the maximum distance ("r") of the cold gas to the geometric center ("O") of the warm layer is "a." The R.A. offset of the geometric center is "X0." The maximum expanding velocity is "V_{max}." Upper panel: the observed line of sight (LOS) expanding velocities at individual positions are plotted as crosses with error bars. The line of sight (LOS) expansion velocity V_{exp}^{los} is defined as $V_{exp}^{los} = V_{emi} - V_{abs}$, where V_{emi} is the velocity of the emission peak of SO$_2$ ($28_{4,24}$–$28_{3,25}$) and V_{abs} is the velocity of the absorption dip of HCO$^+$ (3–2). The two 1.1 mm continuum emission peaks are shown in stars. The best fits to the position–velocity curves are shown in red and blue solid lines, which correspond to [b, a, X0, V_{max}] of [$1''.18$, $2''.84$, $-6''.24$, 3.37 km s^{-1}] and [$1''.43$, $4''.57$, $2''.52$, 5.27 km s^{-1}], respectively.

upper panel of Figure 7. We ignored the positions where the "2.0" and "12.5 km s^{-1}" absorption systems overlaps such as off positions ($-1''.5$, $-1''.5$) and ($-2''.5$, $-1''.5$).

There are two peaks in the "V_{exp}^{los} versus R.A." plot in the upper panel of Figure 7: the eastern one around $2''.5$ and the western one around $-6''$. This "V_{exp}^{los} versus R.A." curve cannot be simply fitted with a spherically expanding model with a constant expansion velocity, in which the position–velocity curve would be elliptical. Instead, we propose a toy model, which is shown in the lower panel of Figure 7, to explain the absorption of HCO$^+$ (3–2). Relative to the warm gas layer that is distributed in the central plane, the two parallel elliptical cold layers are moving outward. The positions of the cold layer can be described with two parameters: height from the central plane ("h") and distance ("r") to the geometric expansion center "O" whose R.A. offset is "X0." The maxima of "h" and "r" are "b" and "a," respectively. Assuming this

simple geometric model, we find that the "V_{exp}^{los} versus R.A." curve can be well-fitted with $V_{exp} \propto r^{-1}$, indicating that the expansion decreases with the distance to the geometric expansion center. V_{exp} is the real expanding velocity: $V_{exp} = \frac{V_{exp}^{los}}{\cos(\theta)}$, where θ is the angle of the velocity vector with respect to the LOS. The maximum expansion velocity V_{max} corresponds to the minimum distance "b." The best fits with the smallest χ^2 are shown in the red and blue solid lines in the upper panel of Figure 7. The parameters [b, a, X0, V_{max}] of the best fits to the western and eastern expansion systems are [$1''.18$, $2''.84$, $-6''.24$, 3.37 km s^{-1}] and [$1''.43$, $4''.57$, $2''.52$, 5.27 km s^{-1}], respectively.

The dynamical timescale can be estimated as $t_{exp} = \frac{b}{V_{max}}$. The dynamical timescales for the western and eastern expansion systems are 1.8×10^4 and 1.4×10^4 year, respectively. The actual masses (M) of the expanding cloud can be roughly estimated from their virial masses M_{vir} (Kauffmann et al. 2013):

$$\frac{M}{10^3 M_\odot} = M_{vir}/\alpha_{cr} = 1.2 \left(\frac{\sigma_v}{km\ s^{-1}} \right)^2 \left(\frac{R_{eff}}{pc} \right) / \alpha_{cr}, \qquad (3)$$

where α_{cr} is the so-called critical virial parameter and is found to be 2 ± 1 for a wide range of cloud shapes and density gradients. Here we take α_{cr} of 2 (Kauffmann et al. 2013). The radius R_{eff} here is taken as an effective radius of $\sqrt{ab}$. The R_{eff} values of the western and eastern expanding clouds are $\sim$0.10 and $\sim$0.14 pc, respectively. Velocity dispersion σ_v is measured from the line width of the absorption lines of HCO$^+$ (3–2). The σ_v is found to be 1.5 and 1.8 km s^{-1} for the western and eastern expanding clouds, respectively. Thus, the masses of the western and eastern expanding clouds are $\sim$270 and $\sim$130 $M_\odot$, respectively. For "subcritical" clouds, which are unbound and expanding, the virial parameter should be larger than the critical virial parameter. Thus, the actual mass estimated from Equation (3) should be taken as an upper limit. We define an effective expanding velocity as $V_{eff} = \frac{b}{R_{eff}} \times V_{max}$. The V_{eff} values of the western and eastern expanding clouds are $\sim$2.2 and $\sim$2.9 km^{-1}, respectively. Then we can estimate the momentum and kinetic energy of the expanding clouds as $P = M \times V_{eff}$ and $E_{kin} = \frac{1}{2} M \times V_{eff}^2$, respectively. The momenta of the western and eastern expanding clouds are $\sim$290 and 790 $M_\odot$ km s^{-1}, respectively. The kinetic energies of the western and eastern expanding clouds are $\sim$6.3 $\times 10^{45}$ and $\sim$2.3 $\times 10^{46}$ erg, respectively. The corresponding mechanical luminosity L_m is calculated as $L_m = E_{kin}/t_{exp}$. The L_m values of the western and eastern expanding clouds are 2.9 and 13.7 $L_\odot$, respectively.

Smith et al. (2009) suggest that the cavity encircled by radio source "G1" to "G5" is caused by the outflow. Assuming an efficiency of 1%–10%, the mechanical heating rate of the outflow is about 13 to 130 $L_\odot$, which is comparable or much larger than the mechanical luminosity of the eastern expanding cloud, indicating that the outflow has sufficient energy to blow the cavity. The extent and timescale of the outflow are also comparable to those of the eastern expanding cloud that is associated with the cavity. All indicate that the cavity is formed due to the outflow. However, this scenario is doubtful because that the outflow appears to have a very small inclination angle

and the outflow lobes are very compact (0.1–0.2 pc in radius). The red outflow lobe is about $2''.7$ ($\sim$0.15 pc) away from the expanding center of the cavity. This displacement is comparable to the radii of outflow lobes and could be resolved by the present SMA beam size ($\sim 2''.4$). On the other hand, we also notice that the stellar wind of an O type star also has sufficient energy to create such a cavity. The mechanical luminosity of an O type star with a mass-loss rate of $10^{-6}\,M_{\odot}\,\mathrm{yr}^{-1}$ and a stellar wind velocity of $2000\,\mathrm{km\,s^{-1}}$ is $\sim$340 $L_{\odot}$. Assuming an efficiency of 10%, its mechanical heating rate is larger than the mechanical luminosity (13.7 $L_{\odot}$) of the eastern expanding cloud. Therefore, we suggest that the expansion of the cavity is more likely due to the mechanical heating produced by the stellar winds rather than the outflow. The western expanding cloud is associated with a radio source "B," which contains one O6.5 and one O5.5 ZAMS type stars (De Pree et al. 2000). The HCO$^+$ lines show typical "P-Cygni" profile toward radio source "B," which indicates the expansion of an H II region.

Two expanding shells with an average radius of $\sim$3.3 pc have been identified with the mid-infrared images and the ^{13}CO $J = 2$–1 and C^{18}O $J = 2$–1 data from the Institute for Radio Astronomy in the Millimeter Range (IRAM) 30-m observations (Peng et al. 2010). The average mass of the expanding shells is $2 \times 10^4\,M_{\odot}$, with a kinetic energy of $\sim 10^{49}$ erg, which are 2 or 3 orders of magnitude larger than the expanding systems reported in this paper. The expansion traced by the HCO$^+$ (3–2) line is more localized when compared with those infrared expanding shells. The connection between HCO$^+$ expansion systems and infrared expanding shells is not clear.

5. SUMMARY

We have studied W49N with the SMA data in the 1.1 mm continuum and molecular line emission. The main results of this study are as follows.

1. Two clumps are revealed in the 1.1 mm continuum emission. The eastern one is very close to radio source "G1" and "G2," and the western clump coincides with the radio source "B."

2. HCN (3–2) lines show extremely high-velocity emission, indicating energetic outflow motions. This is the first report of high-velocity outflow detection in W49N. The total outflow mass is 40 $M_{\odot}$. The total momentum and energy are 1700 $M_{\odot}$ $\mathrm{km\,s^{-1}}$ and 8.7×10^{47} erg, respectively. The dynamic timescale of the outflow is about 0.5–1 $\times 10^4$ year. The total mechanical luminosity and the mass-loss rate are estimated to be $1.3 \times 10^3\,L_{\odot}$ and $5.6 \times 10^{-4}\,M_{\odot} \cdot \mathrm{yr}^{-1}$, respectively. The corresponding accretion rate is at least $1.7 \times 10^{-3}\,M_{\odot} \cdot \mathrm{yr}^{-1}$. The orientation for the high-velocity HCN outflow is opposite to the low-velocity CO outflow, indicating that the outflow jet might be in precession. The jet precession can naturally explain the distribution, velocity, and rotation of water maser spots.

3. Three absorption systems are identified in HCO$^+$ (3–2) spectra, which are at "$-7.5\,\mathrm{km\,s^{-1}}$," "$2.0\,\mathrm{km\,s^{-1}}$," and "$12.5\,\mathrm{km\,s^{-1}}$," respectively. The "$-7.5\,\mathrm{km\,s^{-1}}$" absorption is associated with radio continuum sources "H" and "G4." The "$2.0\,\mathrm{km\,s^{-1}}$" absorption perfectly corresponds to the 3.6 cm continuum emission of "G," which includes sources "G1" to "G5." The "$12.5\,\mathrm{km\,s^{-1}}$" absorption is associated with radio source "B." The absorption of HCO$^+$ (3–2) is blueshifted with respect to the emission of SO$_2$ ($28_{4,24}$–$28_{3,25}$) lines, indicating a cold layer is expanding in front of the warm gas. Analysis toward the "2.0," and "$12.5\,\mathrm{km\,s^{-1}}$" absorption system

indicates that the expansion velocity linearly decreases with the distance to the geometric expansion center. The expansion traced by HCO$^+$ (3–2) absorption features might be caused by mechanical heating of stellar winds from associated O type stars.

REFERENCES

Beuther, H., Schilke, P., Sridharan, T. K., et al. 2002, A&A, 383, 892
Buckley, H. D., & Ward-Thompson, D. 1996, MNRAS, 281, 294
De Pree, C. G., Mehringer, D. M., & Goss, W. M. 1997, ApJ, 482, 307
De Pree, C. G., Wilner, D. J., Goss, W. M., Welch, W. J., & McGrath, E. 2000, ApJ, 540, 308
Galván-Madrid, R., Liu, H. B., Zhang, Z.-Y., et al. 2013, ApJ, 779, 121
Gwinn, C. R., Moran, J. M., & Reid, M. J. 1992, ApJ, 393, 149
Ho, Paul T. P., Moran, J. M., & Lo, K. Y. 2004, ApJL, 616, L1
Honma, M., Yoon, K. C., Bushimata, T., et al. 2004, PASJ, 56, L15
Jørgensen, J. K., Hogerheijde, M. R., Blake, G. A., et al. 2004, A&A, 415, 1021
Kauffmann, J., Pillai, T., & Goldsmith, P. 2013, ApJ, 779, 185
Liu, H. B., Ho, P. T. P., & Zhang, Q. 2010, ApJ, 725, 2190
Liu, T., Wu, Y., Liu, S.-Y., et al. 2011a, ApJ, 730, 102
Liu, T., Wu, Y., Wu, J., Qin, S.-L., & Zhang, H.-W. 2013a, MNRAS, 436, 1335
Liu, T., Wu, Y., & Zhang, H. 2013b, ApJ, 776, 29
Liu, T., Wu, Y., Zhang, Q., et al. 2011b, ApJ, 728, 91
Mac Low, M. M., Elitzur, M., Stone, J. M., & Konigl, A. 1994, ApJ, 427, 914
Mcgrath, E. J., Gross, W. M., & de Pree, C. G. 2004, ApJS, 155, 577
Miyawaki, R., Hayashi, M., & Hasegawa, T. 1986, ApJ, 305, 353
Moran, J. M., Papadopoulos, G. D., Burke, B. F., et al. 1973, ApJ, 185, 535
Mufson, S. L., & Liszt, H. S. 1977, ApJ, 212, 664
Nagy, Z., van der Tak, F. F. S., Fuller, G. A., Spaans, M., & Plume, R. 2012, A&A, 542, 6
Naranjo-Romero, R., Zapata, L. A., Vázquez-Semadeni, E., et al. 2012, ApJ, 757, 58
Peng, T.-C., Wyrowski, F., van der Tak, F. F. S., Menten, K. M., & Walmsley, C. M. 2010, A&A, 520, A84
Qiu, K., Zhang, Q., Megeath, S. T., et al. 2008, ApJ, 685, 1005
Roberts, H., van der Tak, F. F. S., Fuller, G. A., et al. 2011, A&A, 525, 107
Sault, R. J., Teuben, P. J., & Wright, M. C. H. 1995, in ASP Conf. Ser. 77, Astronomical Data Analysis Software and Systems IV, ed. R. A. Shaw et al. (San Francisco, CA: ASP), 433
Scoville, N. Z., Sargent, A. I., Sanders, D. B., et al. 1986, ApJ, 303, 416
Serabyn, E., Guesten, R., & Schulz, A. 1993, ApJ, 413, 571
Shu, F. H., Adam, F. C., & Lizano, S. 1987, ARA&A, 25, 23
Sievers, A. W., Mezger, P. G., Bordeon, M. A., et al. 1991, A&A, 251, 231
Smith, N. 2006, MNRAS, 367, 763
Smith, N., Whitney, B. A., Conti, P. S., De Pree, C. G., & Jackson, J. M. 2009, MNRAS, 399, 952
Su, Y.-N., Liu, S.-Y., Chen, H.-R., Zhang, Q., & Cesaroni, R. 2007, ApJ, 671, 571
Tarter, T. C., & Welch, W. J. 1986, ApJ, 305, 467
Walker, R. C., Matsakis, D. N., & Garcia-Barreto, J. A. 1982, ApJ, 255, 128
Welch, W. J., Dreher, J. W., Jackson, J. M., Terebey, S., & Vogel, S. N. 1987, Sci, 238, 1550
Williams, J. A., Dickel, H. R., & Auer, L. H. 2004, ApJS, 153, 463
Wu, Y., Wei, Y., Zhao, M., et al. 2004, A&A, 426, 503
Zhang, B., Reid, M. J., Menten, K. M., et al. 2013, ApJ, 775, 79
Zhang, Q., Hunter, T. R., Brand, J., et al. 2001, ApJL, 552, L167
Zhang, Q., Hunter, T. R., Brand, J., et al. 2005, ApJ, 625, 864
Zhu, L., Zhao, J.-H., & Wright, M. C. H. 2011, ApJ, 740, 114
Zinnecker, H., & Yorke, H. W. 2007, ARA&A, 45, 481